Air-sea coupling shapes North American hydroclimate response to ice sheets during the Last Glacial Maximum

Dillon J. Amaya[1], Alan M. Seltzer[2], Kristopher B. Karnauskas[1,3], Juan M. Lora[4], Xiyue Zhang[5], and Pedro N. DiNezio[3]

[1]Cooperative Institute for Research in Environmental Sciences, University of Colorado Boulder

[2]Woods Hole Oceanographic Institution

[3]Department of Atmospheric and Oceanic Sciences, University of Colorado Boulder

[4]Department of Earth and Planetary Sciences, Yale University

[5]Department of Earth and Planetary Sciences, Johns Hopkins University

Corresponding author: Dillon J. Amaya, dillon.amaya@colorado.edu, 816-916-8348

Abstract

The Western U.S. is vulnerable to hydrological stress, and insights from past climate periods are helpful for providing historical benchmarks for future climate projections. Myriad evidence from coupled models and paleoclimatic proxies suggests a major reorganization of west coast hydroclimate during the Last Glacial Maximum (LGM, ~17-25 ka), such that the Southwest U.S. was wetter than modern day and the Pacific Northwest was drier. Yet the fundamental mechanisms underlying these hydroclimatic shifts remain unclear. Here, we employ a suite of targeted model simulations to probe the influence of LGM Northern Hemisphere ice sheets on west coast atmospheric dynamics. Whereas previous modeling studies have suggested that the southward shift of LGM west coast precipitation was driven only by the mechanical steering of atmospheric circulation by elevated ice sheet topography, we find this to be an artifact of earlier simulations that neglected realistic air-sea interaction. Instead, our simulations indicate that ice sheet albedo induced a pattern of North Pacific sea surface temperatures, reinforced by ocean-atmosphere feedbacks, that shifted the large-scale atmospheric circulation as well as the latitudinal distribution of west coast precipitation southward during the LGM. Crucially, we find that atmosphere-ocean feedbacks that sustained this ice sheet albedo-induced temperature pattern in the LGM could drive similar hydroclimatic changes today.

Keywords

Last Glacial Maximum; Hydroclimate; Paleoclimate; Climate Modeling; Air-sea Interactions

1 Introduction

The hydroclimate of western North America is heavily influenced by intermittent wintertime storms ("atmospheric rivers") that can produce extreme precipitation, especially when these storms encounter substantial orographic features. For California, in particular, annual water availability hinges on the occurrence of just a handful of such atmospheric river events (Ralph and Dettinger, 2011). This region's acute vulnerability to climate variability and change is exacerbated by its growing human population. Therefore, understanding the fundamental drivers of hydroclimatic change over the west coast of the United States is essential for predicting the future habitability and agricultural viability of this region.

Large amplitude shifts in past climate, beyond the relatively brief instrumental record, provide essential insights into such projections. In this regard, the Last Glacial Maximum (LGM) serves as a useful test case of a relatively recent stable climate state that (a) was substantially different than our present climate and (b) for which we have reasonable constraints on important boundary conditions including orbital geometry, greenhouse gas (GHG) concentrations, sea level, ice volume, etc. To effectively leverage the LGM as a testbed for understanding future change, however, it is necessary to disentangle the climate impacts of forcings that are presently changing (e.g., GHG concentrations) from those that are not (e.g., continental ice sheets).

It has long been suggested that a major non-GHG driver of LGM atmospheric circulation change was the large topographic extent of the ice sheets over North America (Figure 1). Ice sheet forcing has been linked to the dramatic reorganization of west coast hydroclimate during the LGM (Anderson et al., 1988; Broccoli and Manabe, 1987; Cook and Held, 1988; Wong et al., 2016; Yanase and Abe-Ouchi, 2010), which is suggested to have been considerably wetter than present throughout the southwestern U.S. by a preponderance of general circulation model

(GCM) simulations and paleoclimate proxy reconstructions (Anderson et al., 1988; Bartlein et al., 2011; Benson et al., 2011; Ibarra et al., 2014; Kirby et al., 2013; Lachniet et al., 2014; Lemons et al., 1996; Lora et al., 2017; Maher et al., 2014; Oster et al., 2015; Owen et al., 2003; Reheis et al., 2012; Seltzer et al., 2019; Thompson et al., 1999). In particular, coupled model simulations nearly universally indicate a north-south dipole in LGM-to-present precipitation change, such that western North America was wetter in the south and drier in the north (Lora, 2018; Oster et al., 2015).

While models and (to a lesser extent) proxies broadly agree on the existence of this north-south LGM-to-present precipitation dipole response, the physical mechanisms that drove this shift remain an open question. One leading hypothesis is that the North Pacific jet stream was either split or deflected southward, so that extratropical storms and moisture transport occurred further south (Lora et al., 2017). Many studies indicate that the southward deflection of the North Pacific jet may have been the result of mechanical forcing imposed by North American ice sheets, which covered much of modern day Canada and stood ~3 km taller than the present day land surface (Anderson et al., 1988; Bartlein et al., 1998; Bromwich et al., 2004; Cook and Held, 1988; Kim et al., 2008; Kutzbach and Wright, 1985; Manabe and Broccoli, 1985). Other studies point to the dominant influence of high latitude cooling induced by the high albedo of ice sheets (Bhattacharya et al., 2017; Manabe and Broccoli, 1985; Morrill et al., 2018; Roberts et al., 2019; Yanase and Abe-Ouchi, 2010).

Recently, Roberts et al. (2019) found that wintertime atmospheric stationary wave patterns over the North Pacific during the LGM are primarily driven by ice sheet topography, but are enhanced by ice sheet albedo. In contrast, they showed that summertime stationary wave patterns are mainly driven by diabatic heating from the ice sheet albedo with little contribution

from ice sheet topography. In addition, they suggested that ocean dynamics also play a key role in persisting atmospheric circulation anomalies from the summer into the winter. This is consistent with other previous analyses that have broadly implicated ocean-atmosphere coupling as an important factor in modulating the overall response to LGM boundary conditions (DiNezio et al., 2018; Löfverström et al., 2014; Yanase and Abe-Ouchi, 2010).

While these recent studies have provided significant insight into how the different characteristics of the Laurentide and Cordilleran ice sheets may have influenced North Pacific atmospheric circulation, several important questions remain. First, how do different ice sheet-driven stationary wave changes (e.g., Roberts et al. 2019) map onto potential shifts in the North Pacific jet stream? Following from this, do different responses of the zonal circulation to ice sheet topography and ice sheet albedo lead to different hydroclimate shifts along western North America? Additionally, what are the specific ocean dynamical processes and air-sea feedbacks that modulate the seasonally varying response of the North Pacific atmosphere to difference ice sheet boundary conditions?

Here we address these questions by exploring a suite of model simulations (Table 1) conducted with the Community Earth System Model version 1.2 (CESM1) to uncover the drivers and mechanisms of North American west coast hydroclimate change during the LGM, with targeted experiments to distinguish the mechanical (e.g., orographic) and thermodynamic (e.g., albedo-driven) impacts of large continental ice sheets on North Pacific atmospheric circulation. In addition, we build upon Roberts et al. (2019) and others by including a comprehensive range of ocean model complexities, which allow us to directly diagnose the specific ocean-atmosphere interactions and ocean circulation changes that are most relevant to the overall climate response.

2 Data and Methods

2.1 Climate model simulations

The climate model simulations used in this study were conducted by DiNezio et al. (2018). Here, we will provide a broad overview of the major model components, as well as a brief summary of the LGM boundary conditions applied to our various simulations. However, we direct readers to the Supplementary Materials Sections S3-S5 in DiNezio et al. (2018) for a complete description of the climate model components and boundary conditions. Our simulations were carried out using the CESM1 global climate model, which consists of the Community Atmospheric Model version 5 (CAM5; ~2˚ horizontal resolution with 30 vertical pressure levels). CAM5 is coupled to a full-depth ocean model—the Parallel Ocean Program version 2 (POP2)—featuring ~1˚ horizontal resolution, with increased meridional resolution of ~1/3˚ in the tropics, and 60 vertical levels. Additionally, CESM1 features the Community Land Model version 4 (CLM4) with ~2˚ horizontal resolution.

We compare four sets of equilibrated CESM1 experiments with varying degrees of ocean complexity. They include: (1) A fully forced LGM experiment (LGM_{Full}) with all major glacial boundary conditions (GHGs, sea level, orbital, ice sheet topography and albedo, etc.) prescribed following the Paleoclimate Modeling Intercomparison Project Phase III (PMIP3) LGM protocols at 21,000 years ago, (2) A "White Mountain" (WM) simulation that includes all of the LGM ice sheet boundary conditions (e.g., extent, elevation, surface properties), but with the remaining boundary conditions (GHGs, orbit, sea level) set to pre-industrial levels, (3) A "Green Mountain" (GM) simulation that includes identical topography to the WM, but with land surface properties and the remaining boundary conditions set to pre-industrial values, and (4) A pre-industrial control simulation (CTL) with boundary conditions following the PMIP3 pre-industrial

protocols. Figure 1 further illustrates the different LGM and CTL land surface properties used in our experiments.

Ice sheet topography and glacier extent in each of our simulations were prescribed following PMIP3 protocols, which combine three different ice sheet reconstructions (Abe-Ouchi et al., 2015). Otto-Bliesner et al. (2006) showed that the simulated LGM climate in earlier versions of CESM could be sensitive to the choice of ice sheet reconstruction. However, our LGM results do not significantly differ when repeating our analysis using an updated ice sheet reconstruction that is independent of the ice sheet blend used in PMIP3.

The WM and GM experiments include repeated simulations with an atmospheric model that is: (a) uncoupled from the ocean model (AGCM only; i.e., intrinsic atmospheric variability only), (b) coupled to a fixed, 50 m depth slab ocean model (SOM; i.e., no ocean circulation, but ocean-atmosphere interactions possible), and (c) fully coupled to a dynamical ocean model (DOM). In our AGCM experiments, global sea surface temperature (SST) and sea ice extent were prescribed with climatological values from the CTL. Differences among the SOM/DOM and AGCM configurations highlight the role of interactive ocean processes in shaping the overall climate response in the respective GM/WM experiments, while differences between the DOM and SOM isolate the more subtle roles of ocean circulation changes versus mixed layer ocean-atmosphere interactions. (Hereafter we refer to these different experiments and ocean model complexities using the notation "$\text{Experiment}_{\text{model}}$", such as "$\text{WM}_{\text{DOM}}$" for the White Mountain experiment featuring a fully dynamical ocean model). Each of these experiments (summarized in Table 1) was integrated until the climate system (including the deep ocean for DOM simulations) reached close to radiative equilibrium (see DiNezio et al., 2018 Supplenary Materials Section S5

for more details). Each was then integrated forward at equilibrium for an additional number of years (Table 1) to calculate climatological fields for comparison.

Unless otherwise stated, all climate anomalies reported in this study are at least 95% significant using a Student's *t*-test and are relative to a CTL experiment run with the corresponding ocean model complexity. When compared to CTL, atmospheric circulation anomalies in WM are due to the combination of ice sheet albedo and topography (i.e., the combination of mechanical and thermodynamic forcing), while circulation anomalies in GM are due to mechanical forcing from the topography alone. Their difference (WM minus GM) estimates the climate response to ice sheet albedo alone (i.e., thermodynamic forcing only). Differencing WM and GM simulations to isolate the direct ice sheet albedo forcing on the climate system implicitly assumes that ice sheet mechanical and thermodynamic forcing are linearly additive. To assess the validity of this assumption, we analyze an additional albedo-forced CESM1 simulation also conducted by DiNezio et al. (2018). This extra simulation features a dynamical ocean model and was forced with the distribution of continental ice set at LGM values, but over the modern topography. All other boundary conditions (GHGs, orbital, topography, etc.) were set to pre-industrial values. This approach isolates the cooling effect of the albedo of the ice sheets relative to modern topography. Following the naming convention of our other experiments, we refer to this fully coupled simulation as White Plains (WP_{DOM}; Table 1 and Figure 1). By comparing WP_{DOM} anomalies to those from WM_{DOM} we are able to discern whether the elevation of the ice sheet albedo forcing introduces significant nonlinearities in the large-scale climate response.

Finally, to test the sensitivity of our LGM_{Full} results to our choice of model, we compare LGM_{Full} to an ensemble of seven models forced with identical LGM boundary conditions taken from the PMIP3 archive. These models are listed in Table S1.

2.2 Precipitation and sea surface temperature proxy estimates

We validate our simulated hydroclimate results against several proxy estimates of LGM western North American precipitation change, as in Lora et al. (2017). These proxies consist primarily of pollen data (Bartlein et al., 2011), but also include other quantitative precipitation estimates (Ibarra et al., 2014; Lemons et al., 1996; Maher et al., 2014; Thompson et al., 1999). In addition, we compare simulated North Pacific SST anomalies to the gridded proxy estimates generated by Tierney et al. (2020). These estimates combine a large collection of geochemical proxies of SST with an isotope-enabled version of CESM to produce a spatially coherent reconstruction of LGM temperatures using data assimilation. Specifically, we use version 2.0 of their LGM data assimilation runs, which features a wider array of model priors than the original dataset. See Tierney et al. (2020) for more details.

3 Results

Our CESM1 LGM_{Full} experiment produces patterns of North Pacific atmospheric circulation and North American west coast hydroclimate change that compare well with the ensemble mean results of seven PMIP3 models forced with the same LGM boundary conditions (Figure 2). Specifically, both our CESM1 LGM_{Full} simulation and the PMIP3 models produce a clear north-south dipole in boreal winter precipitation anomalies along the North American west coast (Figure 2b,d), such that the Southwestern U.S. is wetter than modern and the Pacific

200 Northwest, from Washington to Alaska, is drier than modern. These similarities are further
201 highlighted by the spatial pattern correlation between our CESM1 LGM_{Full} simulation and the
202 PMIP3 ensemble mean, which is R = 0.92 for the zonal wind anomalies and R = 0.85 for the
203 precipitation change, both significant at 95% confidence.

204 The simulated precipitation anomalies are also highly correlated in space with the proxy
205 reconstructions of LGM-to-present precipitation changes (circles Figure 2b,d and Table S2). The
206 correlation between the proxy estimates and the LGM_{Full} precipitation anomalies at the nearest
207 grid cell is R = 0.67, which is significant at 95% confidence. These precipitation changes are due
208 to an intensified and southward shifted wintertime jet stream, which correspondingly shifts
209 southward the distribution of landfalling North Pacific storms (Figure 2a,c). These model-data
210 comparisons are consistent with many previous studies (Anderson et al., 1988; Bartlein et al.,
211 2011; Ibarra et al., 2014; Lachniet et al., 2014; Lemons et al., 1996; Lora, 2018; Lora et al.,
212 2017; Maher et al., 2014; Oster et al., 2015; Owen et al., 2003; Seltzer et al., 2019; Thompson et
213 al., 1999) and give us confidence in our CESM1 modeling framework.

214

215 *3.1 North Pacific climate response to ice sheet topography*

216 Direct orographic forcing from the ~3 km (Figure 1b) tall North American ice sheets in
217 GM_{AGCM} produces a southward displacement and intensification of the wintertime North Pacific
218 jet, as well as a general tendency for a north-south shift in west coast hydroclimate (Figure 3a-b),
219 which is similar to the coupled response with full LGM forcings (Figure 2a-b). In particular,
220 GM_{AGCM} produces a strong deceleration of the westerlies at ~50˚N (Figure 4a) and throughout
221 the atmospheric column that closely aligns with the latitude at which LGM North American ice
222 sheets begin to rise above modern topography (Figure 4a; orange and purple lines), indicative of

223 a direct mechanical slowdown of the westerly flow ahead of the elevated land surface at these
224 latitudes. The weakened atmospheric circulation is then steered southward, leading to an
225 acceleration of the westerlies near 30˚N. Overall, these zonal wind anomalies produce an
226 equatorward shift of the North Pacific jet stream, especially in the mid-to-lower troposphere.
227 These circulation changes are apparent in the boreal winter geostrophic streamfunction (Figure
228 S1a), which shows an anomalous low over the North Pacific as part of a generally barotropic
229 stationary wave response throughout the Northern Hemisphere, consistent with results presented
230 by Roberts et al. (2019) using a different climate model.

231 Based on the similarities between GM_{AGCM} (Figure 3a-b) and LGM_{Full} (Figure 2a-b), one
232 might reach the same conclusion as many prior AGCM-based studies that also sought to
233 disentangle the role of ice sheet topography versus ice sheet albedo on LGM climate (Anderson
234 et al., 1988; Bartlein et al., 1998; Bromwich et al., 2004; Cook and Held, 1988; Kim et al., 2008;
235 Kutzbach and Wright, 1985; Manabe and Broccoli, 1985)—that ice sheet topography alone is
236 sufficient to explain the overall changes to the LGM North Pacific jet stream, without the need
237 for ocean-atmosphere interactions. However, when coupling our AGCM to interactive ocean
238 models, we in fact find nearly the opposite result. Specifically, both GM_{SOM} and GM_{DOM} show a
239 broad deceleration of the westerlies without a clear latitudinal shift in the jet stream (Figures 3c,e
240 and 4b-c) as well as drier conditions in the Southwestern U.S. relative to the control (Figure
241 3d,f). This raises a key question: What ocean-atmosphere feedbacks and/or ocean circulation
242 changes lead to such markedly divergent circulation and hydroclimate responses between our
243 uncoupled (GM_{AGCM}) and coupled (GM_{SOM} and GM_{DOM}) simulations?

244 Of central importance to addressing this question is the SST warming observed
245 throughout much of the subpolar North Pacific in GM_{DOM} (Figure 5d) and GM_{SOM} (Figure S2a).

These warm anomalies extend upward throughout the atmospheric column (Figure S3b-c), decreasing the meridional temperature gradient between the tropics and the poles, and weakening the North Pacific jet stream by thermal wind balance. An ocean mixed layer heat budget (Supplementary Materials Section S1; Figure S4) indicates that this anomalous subpolar warming can be attributed primarily to three important factors: (1) increased surface shortwave radiation due to decreased low clouds, (2) decreased evaporative cooling driven by the mechanically weakened surface westerlies, and (3) a dynamical ocean response that primarily reflects warm SST advection via Ekman transport (Figure S6a-b). In contrast, without the added atmospheric response to anomalous ocean temperatures, GM_{AGCM} produces cool anomalies in the mid-troposphere near ~40˚N (Figure S3a), consistent with cold air advection from high-latitudes by the anomalous low (Figure S1a). This cooling enhances the local meridional temperature gradient and reinforces the direct mechanical shift of the jet stream, opposite to the behavior observed in GM_{SOM} and GM_{DOM}.

The subpolar warming seen in GM_{DOM} is a robust response to ice sheet mechanical forcing, even when considering the additional impacts of lower LGM GHGs (see Supplementary Materials Section S2). This is because reducing GHGs does not significantly alter the anomalous meridional temperature gradient set up by the direct mechanical ice sheet forcing in GM_{DOM}. However, adding in the full range of altered LGM boundary conditions (including ice sheet albedo) does lead to a much different SST response than in GM_{DOM}. In particular, LGM_{Full} exhibits colder-than-modern conditions throughout the North Pacific (Figure 5c), with the coldest SST anomalies found near the Kuroshio Extension region in a pattern that broadly resembles a positive phase of the Pacific Decadal Oscillation (PDO; Mantua et al., 1997).

This PDO-like cooling is supported by various proxy reconstructions of North Pacific SSTs (Figure 5a) (Gray et al., 2020; Rae et al., 2020; Tao et al., 2013; Tierney et al., 2020), and is also seen in the PMIP3 models analyzed here (Figure 5b and Figure S8) as well as more recent PMIP4-era models (Kageyama et al., 2021). We do note that, while both our LGM_{Full} simulation and the PMIP3 ensemble mean show weak cooling in the subpolar North Pacific, proxy estimates indicate that the subpolar LGM may have been slightly warmer than modern (Rae et al., 2020). Although, these warm anomalies may have been largely confined to a relatively small area north of 50˚N (Figure 5a). Regardless, the broad-scale differences between the ice sheet-driven SST anomalies in our GM_{DOM} and LGM_{Full} experiments further suggest that ocean adjustment to direct mechanical ice sheet forcing (i.e., extensive subpolar North Pacific warming) is not a foundational component of the overall response of the coupled climate system to full LGM boundary conditions.

3.2 North Pacific climate response to ice sheet albedo

We now consider the combined contributions of elevated ice sheet topography (as in GM) and high ice sheet surface albedo to the overall LGM North Pacific climate response. In WM_{AGCM}, the zonal wind and precipitation anomalies are very similar to GM_{AGCM} (Figures 3a-b and 3g-h). Differencing the WM_{AGCM} and GM_{AGCM} simulations, we see little response in the zonal wind and precipitation, thus ice sheet topography is almost entirely responsible for the large-scale atmospheric response in both of these uncoupled simulations (Figures 3m-n). This result is consistent with Roberts et al. (2019), who showed that the wintertime North Pacific stationary wave response to ice sheet topography is similar to the response to ice sheet topography and ice sheet albedo combined (see their Figure 2). Indeed, our WM_{AGCM} and

291 GM_{AGCM} simulations produce nearly identical wintertime stationary wave fields to theirs
292 (Figures S1a and S1g). When coupled to an ocean model in WM_{SOM} and WM_{DOM}, the additional
293 thermodynamic forcing from high ice sheet albedo is responsible for an intensification and
294 southward displacement of the boreal winter North Pacific jet, particularly in the central/eastern
295 North Pacific, leading to the characteristic north-south dipole in western North American
296 precipitation (Figure 3i-l). This can be seen more clearly when differencing the respective WM
297 and GM simulations (Figure 3o-r).

298 To what extent can the differences between our WM and GM simulations be explained
299 by ice sheet albedo versus potential nonlinearities in the climate system? Our WP_{DOM} simulation
300 isolates the climate response to ice sheet albedo relative to modern day topography, and provides
301 a useful tool to address this question. In WP_{DOM}, the boreal winter North Pacific jet experiences
302 an intensification and southward shift that is qualitatively similar to that seen in WM_{DOM} minus
303 GM_{DOM} (Figure S9a,c). This leads to a north-south shift in precipitation in WP_{DOM} that is also
304 comparable to WM_{DOM} minus GM_{DOM} (Figure S9b,d). Similar results are seen when comparing
305 anomalies from WM_{DOM} to the linear combination of anomalies from WP_{DOM} and GM_{DOM}
306 (Figure S9e-h). While the spatial patterns of anomalies between the different ice sheet albedo
307 forcing estimates are qualitatively similar, the zonal wind anomalies in WP_{DOM} tend to be weaker
308 than in WM_{DOM} and the moistening signal in the southwest U.S. is overall less clear in WP_{DOM}.
309 These results suggest that some nonlinearities likely contribute to the differences between our
310 WM and GM simulations and that WM minus GM should not be quantitatively interpreted.
311 Instead, the albedo forcing estimates provided by taking WM minus GM (i.e., Figures 3m-r and
312 4g-i) should be seen as a qualitative indicator of how elevated ice sheet albedo forcing imprints
313 on large-scale climate.

The WP_{DOM} experiment discussed above is an idealized representation of LGM conditions (i.e., it is unlikely that there would ever be such extensive ice sheet albedo forcing across relatively low topography in the real world). However, our WM_{DOM} simulation provides a much more realistic representation of total ice sheet forcing with which to compare to our full LGM simulation. For example, the WM_{SOM} and WM_{DOM} zonal wind and precipitation anomalies are nearly identical to those seen in LGM_{Full} (comparing Figures 2a-b and 3i-l), suggesting that thermodynamic forcing from the bright ice sheets is key in setting the overall LGM North Pacific atmospheric response. However, these anomalies are also heavily reliant upon coupled ocean-atmosphere interactions, as indicated by the difference of WM minus GM zonal wind fields across the different ocean configurations (Figure 3m-r and Figure 4g-i). In particular, ocean-atmosphere coupling enables an albedo-forced acceleration of the westerlies throughout the atmospheric column between ~30-40˚N in WM_{SOM} and WM_{DOM}. This response is only slightly larger in WM_{DOM}, indicating that dynamical ocean circulation changes are of secondary importance to mixed layer air-sea interactions in driving these anomalies. Overall, our experiments suggest that the inclusion of ocean-atmosphere coupling in WM_{SOM} and WM_{DOM} acts to reinforce the mechanically induced southward jet shift implied by the uncoupled WM_{AGCM} (Figure 4g).

How do ocean-atmosphere feedbacks and/or ocean circulation changes combine with the direct atmospheric response to thermodynamic ice sheet forcing to form the wintertime WM_{SOM} and WM_{DOM} North Pacific climate anomalies? Both WM_{DOM} (Figure 5e) and WM_{SOM} (Figure S2b) produce PDO-like SST anomaly patterns that are similar to that seen in proxy estimates, our CESM1 LGM_{Full}, and the PMIP3 ensemble mean (Figure 5a-c). However, the peak anomalies in

336 WM_{DOM}—exceeding -4˚C in magnitude—are only about half as large as in LGM_{Full} since the
337 latter experiences additional cooling from changes in orbital configuration and lower GHGs.
338 Using a mixed layer heat budget analysis, we find that the WM_{DOM} cooling primarily
339 results from: (1) decreases in downward surface shortwave radiation south of 40˚N, (2) ocean
340 circulation changes poleward of 40˚N, and (3) increased evaporation from strengthened surface
341 winds and an increased air-sea temperature contrast (Figure S5). The cooling generated by ocean
342 circulation changes has contributions from anomalous Ekman heat advection (Figure S6c-d), but
343 is also consistent with a southward expansion of the North Pacific subpolar gyre circulation and
344 a southward shift of the subarctic SST front in response to strengthened polar easterlies (Gray et
345 al., 2020). The anomalous temperatures around 40˚N extend throughout much of the atmospheric
346 column to ~300 mb, increasing the meridional temperature gradient over the North Pacific and
347 strengthening the jet stream in WM_{SOM} and WM_{DOM} by thermal wind balance (Figure S3e-f).
348 To confirm that the underlying SST field is indeed driving the boreal winter upper-level
349 zonal wind response, we conducted an additional set of AGCM simulations forced with pre-
350 industrial land surfaces (i.e., no LGM ice sheets) and the long-term monthly mean SST output
351 from WM_{DOM} (referred to as WM_{SST}; see Supplementary Materials Section S3). The consistency
352 between the WM_{SST} global experiment and WM_{DOM} is striking (Figures 4f and 6b), and suggests
353 that nearly the entire LGM North Pacific atmospheric circulation—and thus North American
354 hydroclimatic—response during boreal winter is attributable to the ice sheet-driven SST field
355 and not to the direct atmospheric response to the combined effects of ice sheet orography and
356 albedo (as estimated by WM_{AGCM}). Regional SST forced experiments show that the
357 aforementioned North Pacific SST pattern accounts for the majority of the global SST forced
358 response, particularly the accelerated westerlies between ~30˚-40˚N (Figure 6c-e). Therefore, the

direct atmospheric response to continental ice sheets is only important to the extent that it contributes to the formation of this PDO-like SST pattern (Figure 5e).

3.3 Physical mechanisms linking ice sheet albedo to North Pacific SST changes

The North Pacific ocean and atmosphere are highly coupled in boreal winter (Alexander, 1992; Alexander and Scott, 1997). Therefore, it is important to diagnose the extent to which the SST cooling described above is a source or a symptom of the atmospheric circulation anomalies in the WM experiments. In doing so, we can better understand the physical pathways by which the direct large-scale atmospheric response to a tall/bright ice sheet (as in WM_{AGCM}) first imprints onto the North Pacific ocean before coupling back to the atmosphere (as in WM_{SOM}/WM_{DOM}). The direct thermodynamic impact of North American ice sheets on the large-scale atmosphere should be strongest in boreal summer when the zonal winds are weakest and most sensitive to diabatic heating (Roberts et al., 2019; Ting, 1994). Additionally, anomalous cooling over land caused by high ice sheet albedo will be largest in summer when there is more insolation to reflect.

The seasonally varying influence of ice sheet albedo on large-scale atmospheric circulation was discussed in detail by Roberts et al. (2019), and is reproduced here as the difference between WM and GM stationary wave fields in our AGCM simulations (Figure S1m-r). Importantly, the summertime atmospheric circulation anomalies are more similar across the AGCM/SOM/DOM configurations than those in winter for both WM and GM simulations. The insensitivity of the boreal summer climate response to the presence of an ocean in our simulations suggests that the ocean and the large-scale atmosphere are largely decoupled during this season. This is confirmed in our additional WM_{SST} experiment, which does not reproduce

382 the WM_{DOM} zonal wind anomalies in boreal summer (not shown). Therefore, by relating the WM
383 annual mean SST cooling (Figure 5e) to summer North Pacific climate anomalies, we can
384 reliably diagnose the direct atmospheric response to the tall/bright ice sheet, even in our coupled
385 simulations.

386 As discussed previously, decreases in surface shortwave radiation play an integral role in
387 cooling the North Pacific in WM_{DOM}, with cloud changes accounting for nearly the entire surface
388 shortwave contribution to the SST anomalies (Figure 7a-c). Our simulation shows an increase in
389 total cloud fraction in this region; however, the shortwave cloud radiative forcing (Figure 7b) is
390 primarily due to an increase in low clouds, such as marine stratocumulus (Figure 8a). Low-lying
391 marine stratocumulus clouds are an important amplifying factor for SST anomalies in the North
392 Pacific (Norris et al., 1998; Ronca and Battisti, 1997), often producing a positive feedback with
393 increasing (decreasing) SSTs leading to decreasing (increasing) low cloud amounts and
394 consequently more (less) downward shortwave radiation at the surface (Amaya et al., 2020).

395 Direct ice sheet-driven large-scale atmospheric circulation changes can be connected to
396 local SST anomalies independent of these ocean-atmosphere feedbacks in WM_{AGCM}. This
397 uncoupled simulation produces a strikingly similar pattern of surface shortwave-induced SST
398 anomalies, which are also dominated by changes in shortwave cloud radiative forcing (Figure
399 7d-f). Aside from the similar spatial pattern, the anomalies are generally weaker in WM_{AGCM}
400 than in WM_{DOM}, suggesting that local low cloud-SST feedback amplifies both the low cloud and
401 SST response in WM_{DOM}. Averaging the fractional change in low cloud amount in the central
402 North Pacific, we see that the increase in low clouds in WM_{AGCM} and WM_{DOM} is largest in boreal
403 summer (Figure 7g), with the difference between the two further highlighting the role of ocean-
404 atmosphere feedbacks in amplifying these changes in WM_{DOM} throughout the year.

405 The increase in summertime low cloud coverage in both WM_{AGCM} and WM_{DOM} is due
406 primarily to a stronger temperature inversion above the marine boundary layer west of ~160˚W
407 and increased moisture east of ~160˚W (Figure 8). These changes are driven by an anomalous
408 cyclonic circulation in the lower atmosphere seen in each of our WM simulations during boreal
409 summer (Figure S1j-l). This low pressure anomaly advects cold air from the high latitudes in the
410 western North Pacific (increasing stability at low levels), while advecting additional moisture
411 from the tropics in the eastern North Pacific. See Supplementary Materials Section S1.4 for more
412 details on the cloud parameters analyzed here.

413 Overall, the consistent change in cloudiness in the WM_{AGCM} simulation provides
414 evidence that the direct large-scale atmospheric response to North American ice sheets first
415 influences North Pacific SSTs during boreal summer through changes in cloud fraction and
416 surface shortwave radiation. These SST anomalies then persist into winter through a combination
417 of positive feedbacks including low cloud-SST and wind-evaporation-SST interactions, as well
418 as ocean circulation adjustments, where they then strongly influence the position of the North
419 Pacific jet and, by extension, North American west coast hydroclimate.

420

421 ## 4 Summary

422 In this study, we investigated the influence of continental ice sheets on North Pacific
423 atmospheric circulation and North American west coast hydroclimate during the LGM. Our
424 model results showed that, in response to full LGM boundary conditions (e.g., GHGs, ice sheets,
425 sea level, orbital configuration, etc.), the North Pacific jet is intensified and shifted southward
426 during boreal winter. This results in a wetter-than-modern-day Southwest U.S. and a drier-than-
427 modern-day Pacific Northwest, consistent with previous model simulations and paleoproxy

reconstructions (Anderson et al., 1988; Bartlein et al., 2011; Benson et al., 2011; Ibarra et al., 2014; Kirby et al., 2013; Lachniet et al., 2014; Lemons et al., 1996; Lora et al., 2017; Maher et al., 2014; Oster et al., 2015; Owen et al., 2003; Reheis et al., 2012; Seltzer et al., 2019; Thompson et al., 1999). Decomposing this climate response into contributions from ice sheet topography alone (i.e., Green Mountain) and ice sheet topography plus albedo (i.e., White Mountain), we found that these circulation changes result from a complex combination of mechanical and thermodynamic ice sheet effects that are critically dependent on the presence of ocean-atmosphere interactions.

The step-by-step response of the North Pacific atmosphere to realistic continental ice sheets (i.e., a White Mountain) is summarized in the schematic Figure 9. In short, the large-scale stationary wave response to tall/bright ice sheets includes a low-level cyclonic circulation over the North Pacific during boreal summer, supported also by previous studies (Roberts et al., 2019). This circulation anomaly increases moisture transport to the eastern North Pacific, while simultaneously advecting cool air from high-latitudes over the western North Pacific. The increase in moisture combined with the increased lower atmosphere stability leads to an increase in low clouds, which cool North Pacific SSTs between 30˚N-40˚N by reducing downward surface shortwave radiation. A positive low cloud-SST feedback and subpolar gyre dynamical adjustments (Gray et al., 2020) then combine to amplify both the cloud changes and the North Pacific SST anomalies, allowing them to persist into boreal winter. During the winter, the ocean couples back to the large-scale atmosphere and reinforces the tendency for a topographically-forced southward shift of the North Pacific jet stream by increasing the North Pacific meridional temperature gradient and accelerating the westerlies on the equatorward flank of the jet.

5 Discussion

Many of the above results are consistent with previous studies (e.g., Roberts et al., 2019; Yanase and Abe-Ouchi, 2010), who used similar model simulations to investigate the importance of different ice sheet characteristics to LGM atmospheric circulation as well as the influence of ocean coupling in shaping those responses. However, our detailed analysis of North Pacific SST patterns helps to fill a notable gap in our understanding of the specific physical pathways (e.g., low cloud feedbacks) by which the coupled climate system adjusts to LGM ice sheet forcing, and helps to further highlight the relevance of LGM climate for modern applications. In particular, our finding that ice sheet-driven SST patterns—rather than the direct atmospheric response to mechanical forcing induced by the elevated topography of the LGM ice sheets—drove much of the North Pacific atmospheric circulation response during the LGM has key implications for present day climate variability and future change.

We suggest that the primary role of ice sheets on LGM hydroclimate was to provide a suitably large perturbation to the climate system that led to the formation of an SST pattern that bears strong resemblance to a well-known climatic mode (e.g., the PDO). In this sense, while the presence (or removal) of a ~3 km tall ice sheet over North America bears no direct relevance to modern climate, the possible emergence of North Pacific SST anomalies that are similar in pattern and magnitude as those observed in our LGM simulations is distinctly plausible. While such patterns may result from natural climate variations, our findings call attention to ongoing anthropogenic factors—such as changes in Southeast Asian aerosol emissions—that have been shown to promote a PDO-like SST response in coupled models (Smith et al., 2016) and may exert a strong influence on western North American hydroclimate through air-sea interactions. These regional SST patterns may further serve to alter the expected response of the mid-latitude

jet streams to future global warming (Lu et al., 2008), due to the modification of the local meridional temperature gradient at the surface.

Finally, we acknowledge several important caveats and possible sensitives regarding our analysis. For example, we note that our analysis is primarily based on simulations from a single model—CESM1.2. However, portions of our results (particularly the large-scale atmospheric circulation changes associated with different ice sheet characteristics) are nearly identical to Roberts et al. (2019), who conducted similar White Mountain and Green Mountain experiments using a different climate model. Indeed, the North Pacific stationary wave patterns in our simulations (Figure S1) compare very well to those seen in their simulations (see Roberts et al. 2019, Figures 2 and 3). Therefore, we have confidence that the ice sheet-driven atmospheric circulation changes discussed here are qualitatively insensitive to model choice.

Additionally, although we have identified a series of physically consistent pathways by which the coupled climate system adjusts to ice sheet forcing (Figure 9), we note that these mechanisms depend on an accurate representation of marine stratocumulus clouds and their feedbacks. While the simulation of marine stratocumulus clouds has improved in recent model generations (Engström et al., 2014), there is still large uncertainty among models in the expected response of clouds to future greenhouse gas increase (Qu et al., 2014; Webb et al., 2013). Nevertheless, Xiao et al., (2014) showed that CESM1 credibly reproduces the climate conditions necessary to accurately simulate marine stratocumulus clouds in the North Pacific, including the depth of the planetary boundary layer, which gives us confidence in our results. Regardless, future work is needed to further explore the physical mechanisms identified here across a range of other model configurations

Acknowledgements

We thank Shang-Ping Xie and Clara Deser for their helpful comments and suggestions during the course of this study. We also thank Simmi Sinha for her assistance in designing Figure 9. We would like to acknowledge high-performance computing support from Cheyenne (doi:10.5065/D6RX99HX) provided by NCAR's Computational and Information Systems Laboratory, sponsored by the NSF. D.J.A. is funded by a Postdoctoral Fellowship with the Cooperative Institute for Research in Environmental Sciences (CIRES) at the University of Colorado Boulder. P.N.D. was supported by NSF (AGS 2002528). A.M.S. was funded by NSF (OCE-1923915). This work was also supported by NSF (EAR 2102984). The PMIP3 data listed in Table S2 are available at https://esgf-node.llnl.gov/projects/esgf-llnl/. The proxy precipitation data and associated uncertainties are available in Table S2. The data assimilated SST proxy estimates are from Tierney et al. (2020) and are available at https://github.com/jesstierney/lgmDA. The CESM1 simulations originally developed by DiNezio et al. (2018) and analyzed here are available at https://doi.org/10.5281/zenodo.4632397. The additional WM_{SST} CAM5 simulations are available at https://doi.org/10.5281/zenodo.4632424. The figures and analyses were produced with MATLAB. MATLAB code used to perform this analysis is available from the corresponding author upon request. All data needed to evaluate the conclusions in the paper are present in the Supporting Information or at the data repositories listed above. Additional data related to this paper may be requested from the authors.

References

Abe-Ouchi, A., Saito, F., Kageyama, M., Braconnot, P., Harrison, S.P., Lambeck, K., Otto-Bliesner, B.L., Peltier, W.R., Tarasov, L., Peterschmitt, J.Y., Takahashi, K., 2015. Ice-sheet configuration in the CMIP5/PMIP3 Last Glacial Maximum experiments. Geosci. Model Dev. 8, 3621–3637. https://doi.org/10.5194/gmd-8-3621-2015

Alexander, M.A., 1992. Midlatitude atmosphere-ocean interaction during El Niño. Part I: The North Pacific ocean. J. Clim. 5, 944–958. https://doi.org/10.1175/1520-0442(1992)005<0944:MAIDEN>2.0.CO;2

Alexander, M.A., Scott, J.D., 1997. Surface flux variability over the North Pacific and North Atlantic oceans. J. Clim. 10, 2963–2978. https://doi.org/10.1175/1520-0442(1997)010<2963:SFVOTN>2.0.CO;2

Amaya, D.J., Miller, A.J., Xie, S.-P., Kosaka, Y., 2020. Physical drivers of the summer 2019 North Pacific marine heatwave. Nat. Commun. 11, 1903. https://doi.org/10.1038/s41467-020-15820-w

Anderson, P.M., Barnosky, C.W., Bartlein, P.J., Behling, P.J., Brubaker, L., Cushing, E.J., Dodson, J., Dworetsky, B., Guetter, P.J., Harrison, S.P., Huntley, B., Kutzbach, J.E., Markgraf, V., Marvel, R., McGlone, M.S., Mix, A., Moar, N.T., Morley, J., Perrott, R.A., Peterson, G.M., Prell, W.L., Prentice, I.C., Ritchie, J.C., Roberts, N., Ruddiman, W.F., Salinger, M.J., Spaulding, W.G., Street-Perrott, F.A., Thompson, R.S., Wang, P.K., Webb, T., Winkler, M.G., Wright, H.E., 1988. Climatic changes of the last 18,000 years: Observations and model simulations. Science (80-.). 241, 1043–1052. https://doi.org/10.1126/science.241.4869.1043

Bartlein, P.J., Anderson, K.H., Anderson, P.M., Edwards, M.E., Mock, C.J., Thompson, R.S.,

539 Webb, R.S., Webb, T., Whitlock, C., 1998. Paleoclimate simulations for North America
540 over the past 21,000 years: Features of the simulated climate and comparisons with
541 paleoenvironmental data. Quat. Sci. Rev. 17, 549–585. https://doi.org/10.1016/S0277-
542 3791(98)00012-2
543 Bartlein, P.J., Harrison, S.P., Brewer, S., Connor, S., Davis, B.A.S., Gajewski, K., Guiot, J.,
544 Harrison-Prentice, T.I., Henderson, A., Peyron, O., Prentice, I.C., Scholze, M., Seppä, H.,
545 Shuman, B., Sugita, S., Thompson, R.S., Viau, A.E., Williams, J., Wu, H., 2011. Pollen-
546 based continental climate reconstructions at 6 and 21 ka: A global synthesis. Clim. Dyn. 37,
547 775–802. https://doi.org/10.1007/s00382-010-0904-1
548 Benson, L. V., Lund, S.P., Smoot, J.P., Rhode, D.E., Spencer, R.J., Verosub, K.L., Louderback,
549 L.A., Johnson, C.A., Rye, R.O., Negrini, R.M., 2011. The rise and fall of Lake Bonneville
550 between 45 and 10.5 ka. Quat. Int. 235, 57–69. https://doi.org/10.1016/j.quaint.2010.12.014
551 Bhattacharya, T., Tierney, J.E., DiNezio, P., 2017. Glacial reduction of the North American
552 Monsoon via surface cooling and atmospheric ventilation. Geophys. Res. Lett. 44, 5113–
553 5122. https://doi.org/10.1002/2017GL073632
554 Broccoli, A.J., Manabe, S., 1987. The influence of continental ice, atmospheric CO2, and land
555 albedo on the climate of the last glacial maximum. Clim. Dyn. 1, 87–99.
556 https://doi.org/10.1007/BF01054478
557 Bromwich, D.H., Toracinta, E.R., Wej, H., Oglesby, R.J., Fastook, J.L., Hughes, T.J., 2004.
558 Polar MM5 simulations of the winter climate of the Laurentide Ice Sheet at the LGM. J.
559 Clim. 17, 3415–3433. https://doi.org/10.1175/1520-
560 0442(2004)017<3415:PMSOTW>2.0.CO;2
561 Cook, K.H., Held, I.M., 1988. Stationary Waves of the Ice Age Climate. J. Clim. 1, 807–819.

562 https://doi.org/10.1175/1520-0442(1988)001<0807:swotia>2.0.co;2
563 DiNezio, P.N., Tierney, J.E., Otto-Bliesner, B.L., Timmermann, A., Bhattacharya, T.,
564 Rosenbloom, N., Brady, E., 2018. Glacial changes in tropical climate amplified by the
565 Indian Ocean. Sci. Adv. 4. https://doi.org/10.1126/sciadv.aat9658
566 Engström, A., Bender, F.A.M., Karlsson, J., 2014. Improved representation of marine
567 stratocumulus cloud shortwave radiative properties in the CMIP5 climate models. J. Clim.
568 27, 6175–6188. https://doi.org/10.1175/JCLI-D-13-00755.1
569 Gray, W.R., Wills, R.C.J., Rae, J.W.B., Burke, A., Ivanovic, R.F., Roberts, W.H.G., Ferreira, D.,
570 Valdes, P.J., 2020. Wind-Driven Evolution of the North Pacific Subpolar Gyre Over the
571 Last Deglaciation. Geophys. Res. Lett. 47. https://doi.org/10.1029/2019GL086328
572 Ibarra, D.E., Egger, A.E., Weaver, K.L., Harris, C.R., Maher, K., 2014. Rise and fall of late
573 Pleistocene pluvial lakes in response to reduced evaporation and precipitation: Evidence
574 from Lake Surprise, California. Bull. Geol. Soc. Am. 126, 1387–1415.
575 https://doi.org/10.1130/B31014.1
576 Kageyama, M., Harrison, S., Kapsch, M.-L., Löfverström, M., Lora, J., Mikolajewicz, U.,
577 Sherriff-Tadano, S., Vadsaria, T., Abe-Ouchi, A., Bouttes, N., Chandan, D., LeGrande, A.,
578 Lhardy, F., Lohmann, G., Morozova, P., Ohgaito, R., Peltier, W.R., Quiquet, A., Roche, D.,
579 Shi, X., Schmittner, A., Tierney, J., Volodin, E., 2021. The PMIP4-CMIP6 Last Glacial
580 Maximum experiments: preliminary results and comparison with the PMIP3-CMIP5
581 simulations. Clim. Past Discuss. 1–37. https://doi.org/10.5194/cp-2019-169
582 Kim, S.J., Crowley, T.J., Erickson, D.J., Govindasamy, B., Duffy, P.B., Lee, B.Y., 2008. High-
583 resolution climate simulation of the last glacial maximum. Clim. Dyn. 31, 1–16.
584 https://doi.org/10.1007/s00382-007-0332-z

585 Kirby, M.E., Feakins, S.J., Bonuso, N., Fantozzi, J.M., Hiner, C.A., 2013. Latest Pleistocene to
586 Holocene hydroclimates from Lake Elsinore, California. Quat. Sci. Rev.
587 https://doi.org/10.1016/j.quascirev.2013.05.023
588 Kutzbach, J.E., Wright, H.E., 1985. Simulation of the climate of 18,000 years BP: Results for the
589 North American/North Atlantic/European sector and comparison with the geologic record
590 of North America. Quat. Sci. Rev. 4, 147–187. https://doi.org/10.1016/0277-
591 3791(85)90024-1
592 Lachniet, M.S., Denniston, R.F., Asmerom, Y., Polyak, V.J., 2014. Orbital control of western
593 North America atmospheric circulation and climate over two glacial cycles. Nat. Commun.
594 5. https://doi.org/10.1038/ncomms4805
595 Lemons, D.R., Milligan, M.R., Chan, M.A., 1996. Paleoclimatic implications of late Pleistocene
596 sediment yield rates for the Bonneville Basin, northern Utah. Palaeogeogr. Palaeoclimatol.
597 Palaeoecol. 123, 147–159. https://doi.org/10.1016/0031-0182(95)00117-4
598 Löfverström, M., Caballero, R., Nilsson, J., Kleman, J., 2014. Evolution of the large-scale
599 atmospheric circulation in response to changing ice sheets over the last glacial cycle. Clim.
600 Past 10, 1453–1471. https://doi.org/10.5194/cp-10-1453-2014
601 Lora, J.M., 2018. Components and mechanisms of hydrologic cycle changes over North America
602 at the Last Glacial Maximum. J. Clim. 31, 7035–7051. https://doi.org/10.1175/JCLI-D-17-
603 0544.1
604 Lora, J.M., Mitchell, J.L., Risi, C., Tripati, A.E., 2017. North Pacific atmospheric rivers and their
605 influence on western North America at the Last Glacial Maximum. Geophys. Res. Lett. 44,
606 1051–1059. https://doi.org/10.1002/2016GL071541
607 Lu, J., Chen, G., Frierson, D.M.W., 2008. Response of the zonal mean atmospheric circulation to

608 El Niño versus global warming. J. Clim. 21, 5835–5851.
609 https://doi.org/10.1175/2008JCLI2200.1
610 Maher, K., Ibarra, D.E., Oster, J.L., Miller, D.M., Redwine, J.L., Reheis, M.C., Harden, J.W.,
611 2014. Uranium isotopes in soils as a proxy for past infiltration and precipitation across the
612 western United States. Am. J. Sci. 314, 821–857. https://doi.org/10.2475/04.2014.01
613 Manabe, S., Broccoli, A.J., 1985. The influence of continental ice sheets on the climate of an ice
614 age. J. Geophys. Res. 90, 2167–2190. https://doi.org/10.1029/JD090iD01p02167
615 Mantua, N.J., Hare, S.R., Zhang, Y., Wallace, J.M., Francis, R.C., 1997. A Pacific Interdecadal
616 Climate Oscillation with Impacts on Salmon Production. Bull. Am. Meteorol. Soc. 78,
617 1069–1079. https://doi.org/10.1175/1520-0477(1997)078<1069:APICOW>2.0.CO;2
618 Morrill, C., Lowry, D.P., Hoell, A., 2018. Thermodynamic and Dynamic Causes of Pluvial
619 Conditions During the Last Glacial Maximum in Western North America. Geophys. Res.
620 Lett. 45, 335–345. https://doi.org/10.1002/2017GL075807
621 Norris, J.R., Zhang, Y., Wallace, J.M., 1998. Role of low clouds in summertime atmosphere-
622 ocean interactions over the North Pacific. J. Clim. 11, 2482–2490.
623 https://doi.org/10.1175/1520-0442(1998)011<2482:ROLCIS>2.0.CO;2
624 Oster, J.L., Ibarra, D.E., Winnick, M.J., Maher, K., 2015. Steering of westerly storms over
625 western North America at the Last Glacial Maximum. Nat. Geosci. 8, 201–205.
626 https://doi.org/10.1038/ngeo2365
627 Otto-Bliesner, B.L., Brady, E.C., Clauzet, G., Tomas, R., Levis, S., Kothavala, Z., 2006. Last
628 glacial maximum and Holocene climate in CCSM3. J. Clim. 19, 2526–2544.
629 https://doi.org/10.1175/JCLI3748.1
630 Owen, L.A., Finkel, R.C., Minnich, R.A., Perez, A.E., 2003. Extreme southwestern margin of

late Quaternary glaciation in North America: Timing and controls. Geology 31, 729–732. https://doi.org/10.1130/G19561.1

Qu, X., Hall, A., Klein, S.A., Caldwell, P.M., 2014. On the spread of changes in marine low cloud cover in climate model simulations of the 21st century. Clim. Dyn. 42, 2603–2626. https://doi.org/10.1007/s00382-013-1945-z

Rae, J.W.B., Gray, W.R., Wills, R.C.J., Eisenman, I., Fitzhugh, B., Fotheringham, M., Littley, E.F.M., Rafter, P.A., Rees-Owen, R., Ridgwell, A., Taylor, B., Burke, A., 2020. Overturning circulation, nutrient limitation, and warming in the Glacial North Pacific. Sci. Adv. 6. https://doi.org/10.1126/sciadv.abd1654

Ralph, F.M., Dettinger, M.D., 2011. Storms, floods, and the science of atmospheric rivers. Eos (Washington. DC). 92, 265–266. https://doi.org/10.1029/2011EO320001

Reheis, M.C., Bright, J., Lund, S.P., Miller, D.M., Skipp, G., Fleck, R.J., 2012. A half-million-year record of paleoclimate from the Lake Manix Core, Mojave Desert, California. Palaeogeogr. Palaeoclimatol. Palaeoecol. 365–366, 11–37. https://doi.org/10.1016/j.palaeo.2012.09.002

Roberts, W.H.G., Li, C., Valdes, P.J., 2019. The mechanisms that determine the response of the Northern Hemisphere's stationary waves to North American ice sheets. J. Clim. 32, 3917–3940. https://doi.org/10.1175/JCLI-D-18-0586.1

Ronca, R.E., Battisti, D.S., 1997. Anomalous sea surface temperatures and local air-sea energy exchange on intraannual timescales in the northeastern subtropical pacific. J. Clim. 10, 102–117. https://doi.org/10.1175/1520-0442(1997)010<0102:ASSTAL>2.0.CO;2

Seltzer, A.M., Ng, J., Danskin, W.R., Kulongoski, J.T., Gannon, R.S., Stute, M., Severinghaus, J.P., 2019. Deglacial water-table decline in Southern California recorded by noble gas

654 isotopes. Nat. Commun. 10. https://doi.org/10.1038/s41467-019-13693-2
655 Smith, D.M., Booth, B.B.B., Dunstone, N.J., Eade, R., Hermanson, L., Jones, G.S., Scaife, A.A.,
656 Sheen, K.L., Thompson, V., 2016. Role of volcanic and anthropogenic aerosols in the
657 recent global surface warming slowdown. Nat. Clim. Chang. 6, 936–940.
658 https://doi.org/10.1038/nclimate3058
659 Tao, W., Yi, L., Wei, H., 2013. Last Glacial Maximum Sea Surface Temperatures: A Model-
660 Data Comparison. Atmos. Ocean. Sci. Lett. 6, 233–239. https://doi.org/10.3878/j.issn.1674-
661 2834.13.0019
662 Thompson, R.S., Anderson, K.H., Bartlein, P.J., 1999. Quantitative paleoclimatic reconstructions
663 from late Pleistocene plant macrofossils of the Yucca Mountain region, U.S. Geological
664 Survey Open-File Report.
665 Tierney, J.E., Zhu, J., King, J., Malevich, S.B., Hakim, G.J., Poulsen, C.J., 2020. Glacial cooling
666 and climate sensitivity revisited. Nature 584, 569–573. https://doi.org/10.1038/s41586-020-
667 2617-x
668 Ting, M., 1994. Maintenance of Northern Summer Stationary Waves in a GCM. J. Atmos. Sci.
669 51, 3286–3308. https://doi.org/10.1175/1520-0469(1994)051<3286:monssw>2.0.co;2
670 Webb, M.J., Lambert, F.H., Gregory, J.M., 2013. Origins of differences in climate sensitivity,
671 forcing and feedback in climate models. Clim. Dyn. 40, 677–707.
672 https://doi.org/10.1007/s00382-012-1336-x
673 Wong, C.I., Potter, G.L., Montañez, I.P., Otto-Bliesner, B.L., Behling, P., Oster, J.L., 2016.
674 Evolution of moisture transport to the western U.S. during the last deglaciation. Geophys.
675 Res. Lett. 43, 3468–3477. https://doi.org/10.1002/2016GL068389
676 Xiao, H., Mechoso, C.R., Sun, R., Han, J., Pan, H.L., Park, S., Hannay, C., Bretherton, C.,

677 Teixeira, J., 2014. Diagnosis of the marine low cloud simulation in the NCAR community
678 earth system model (CESM) and the NCEP global forecast system (GFS)-modular ocean
679 model v4 (MOM4) coupled model. Clim. Dyn. 43, 737–752.
680 https://doi.org/10.1007/s00382-014-2067-y
681 Yanase, W., Abe-Ouchi, A., 2010. A numerical study on the atmospheric circulation over the
682 midlatitude North Pacific during the last glacial maximum. J. Clim. 23, 135–151.
683 https://doi.org/10.1175/2009JCLI3148.1
684

685 **Table 1** List of the CESM1 experiments used in this study. Crosses indicate the boundary
686 condition has been modified following PMIP3 protocols. All boundary conditions have been
687 applied globally. The availability of dynamical ocean model (DOM), slab ocean model (SOM),
688 or AGCM data is noted in parentheses. The equilibration period for each DOM run is shown in
689 the far right column. The column second from right indicates the additional integration period
690 used for calculating climatologies once each DOM run had reached close to radiative
691 equilibrium. Each SOM and AGCM simulation was spun-up for 10 years, and integrated for an
692 additional 100 years for calculating climatologies. See DiNezio et al. (2018) for complete details
693 regarding the initial conditions and the boundary conditions.

	GHGs	Orbit	Land mask & bathymetry	Topography	Albedo	Duration (yrs)	Equilibration (yrs)
LGM_{Full} (DOM)	X	X	X	X	X	600	500
White Mountain (DOM, SOM, AGCM)				X	X	400	700
Green Mountain (DOM, SOM, AGCM)				X		200	100
White Plains (DOM)					X	400	500

694

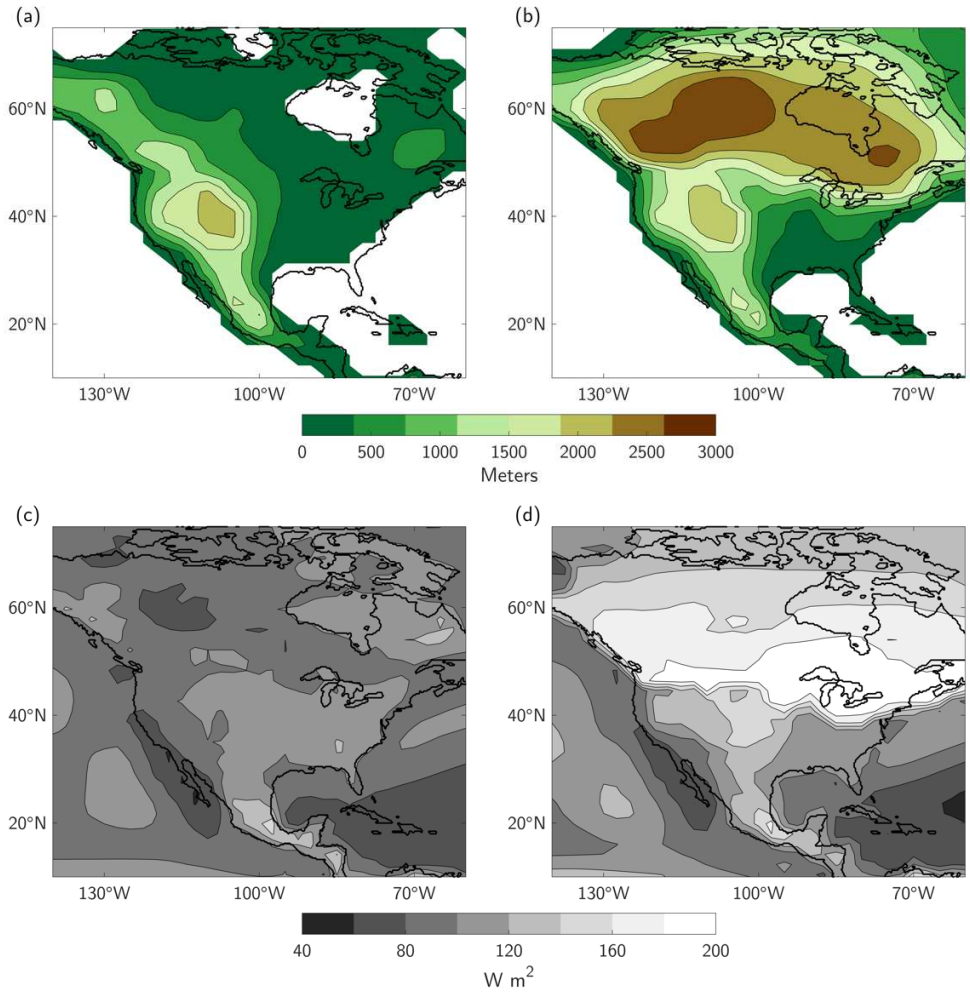

Figure 1 Ice sheet characteristics in our CESM1 simulations. (a)-(b) Surface geopotential divided by 9.8 m/s^2 (meters) and (c)-(d) annual mean upward shortwave radiation at the top of the atmosphere (W m^{-2}) in our CTL (left column) and LGM (right column) simulations. LGM$_{Full}$ and WM simulations have the ice sheet surface properties of (b) and (d) (i.e., tall and bright). GM simulations have the ice sheet surface properties of (b) and (c) (i.e., tall and dark). WP simulations have the ice sheet surface properties of (a) and (d) (i.e., flat and bright).

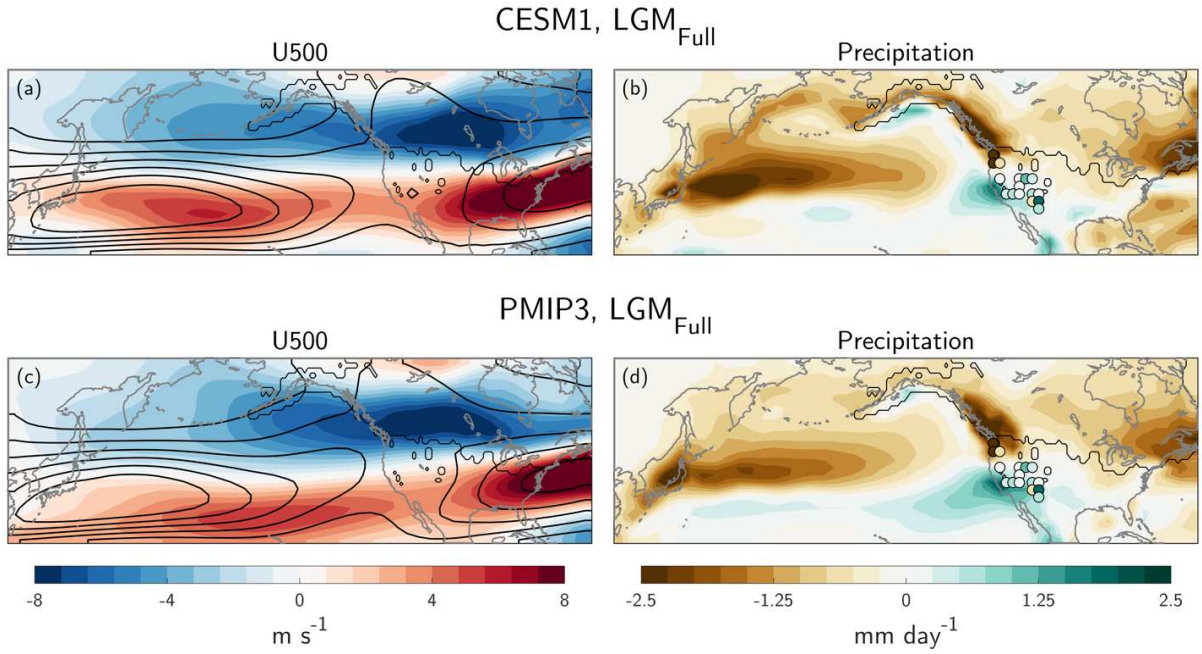

703

704 **Figure 2** North Pacific climate at the Last Glacial Maximum. Difference maps of LGM_{Full} minus
705 CTL (a) 500 mb zonal wind (U500; m s^{-1}) and (b) precipitation (mm day^{-1}) averaged during
706 boreal winter (December-February). Thick black contours in (a) show wintertime U500
707 climatology in the pre-industrial control (contour interval is 5 m s^{-1} with max value of 30 m s^{-1}).
708 (c)-(d) As in (a)-(b), but for the ensemble mean of seven PMIP3 models forced with full LGM
709 boundary conditions minus their respective pre-industrial control simulations. Thin black contour
710 in each panel marks approximate ice sheet edge at the LGM. Filled circles in (b) and (d) show
711 precipitation changes from proxy estimates (Table S2).

712

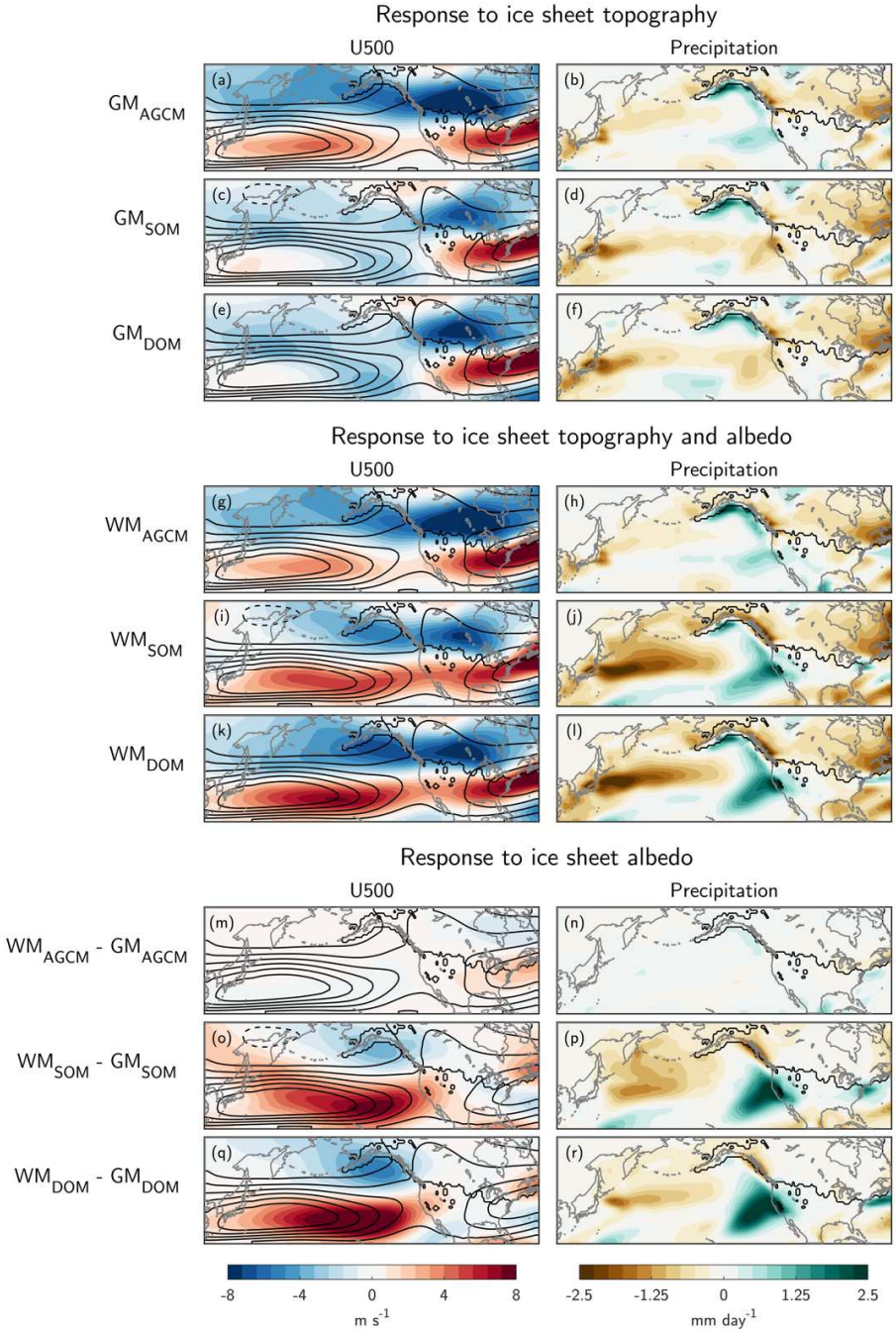

713

714 **Figure 3** North Pacific boreal winter response of 500 mb zonal wind (U500) and precipitation in
715 single forcing experiments: (a)–(f) GM−CTL, (g)-(i) WM−CTL, and (m)–(r) WM−GM in their
716 respective ocean configurations. Thick black contours in show wintertime U500 climatology in
717 the pre-industrial control (contour interval is 5 m s^{-1} with max value of 30 m s^{-1}).

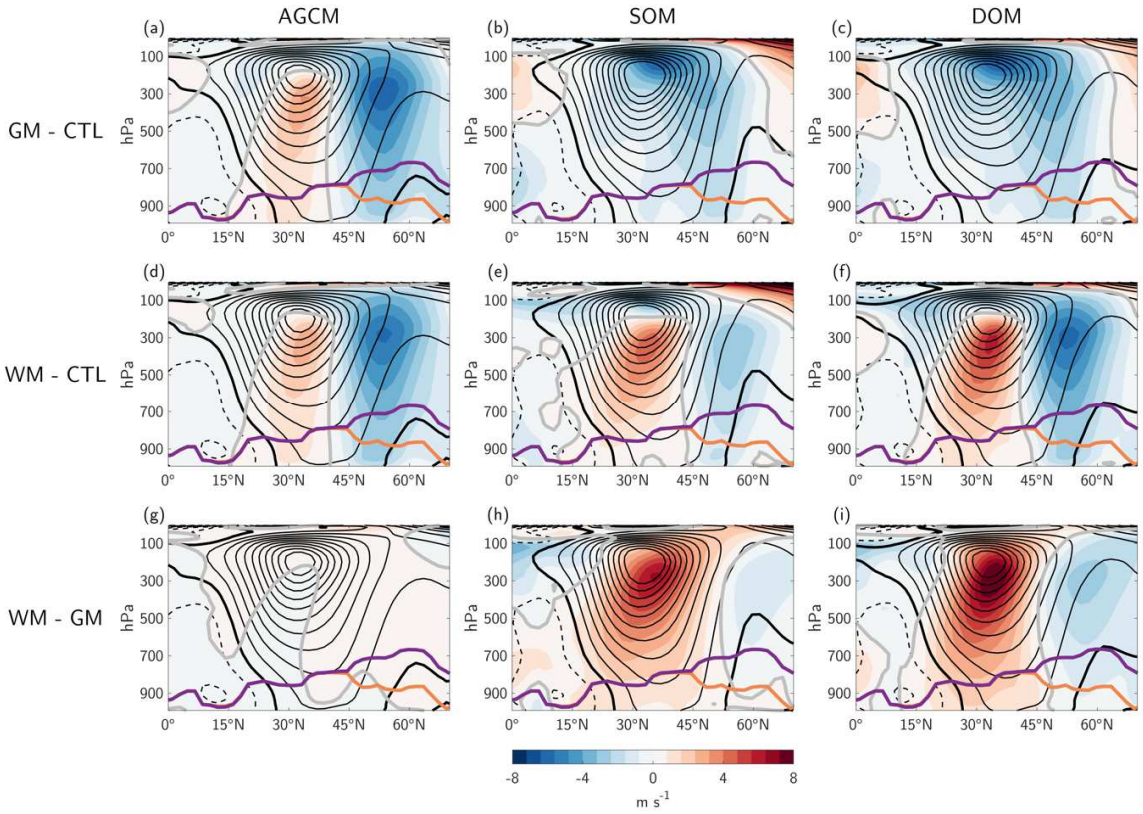

718

719 **Figure 4** North Pacific zonal wind response. Latitude-height cross-sections of boreal winter
720 (December-February) zonal wind anomalies (shading; m s^{-1}) zonally averaged over the Pacific
721 basin (120˚E-110˚W). Anomalies are for (a)-(c) GM minus CTL, (d)-(f) WM minus CTL, and
722 (g)-(i) WM minus GM in their respective (left column) AGCM, (middle column) SOM, and
723 (right column) DOM ocean configurations. Purple and orange contours roughly outline the
724 profile of North American topography at each latitude (i.e., as if looking westward from the
725 Atlantic Ocean) for LGM and CTL, respectively. Black contours denote the winter CTL zonal
726 wind climatology for this region. Solid (dashed) black contours denote positive (negative)
727 values. Black contour interval is 5 m s^{-1} starting at 0 m s^{-1} (thick black contour). Thick gray
728 contour marks the 0 m s^{-1} zonal wind anomaly contour.

729
730

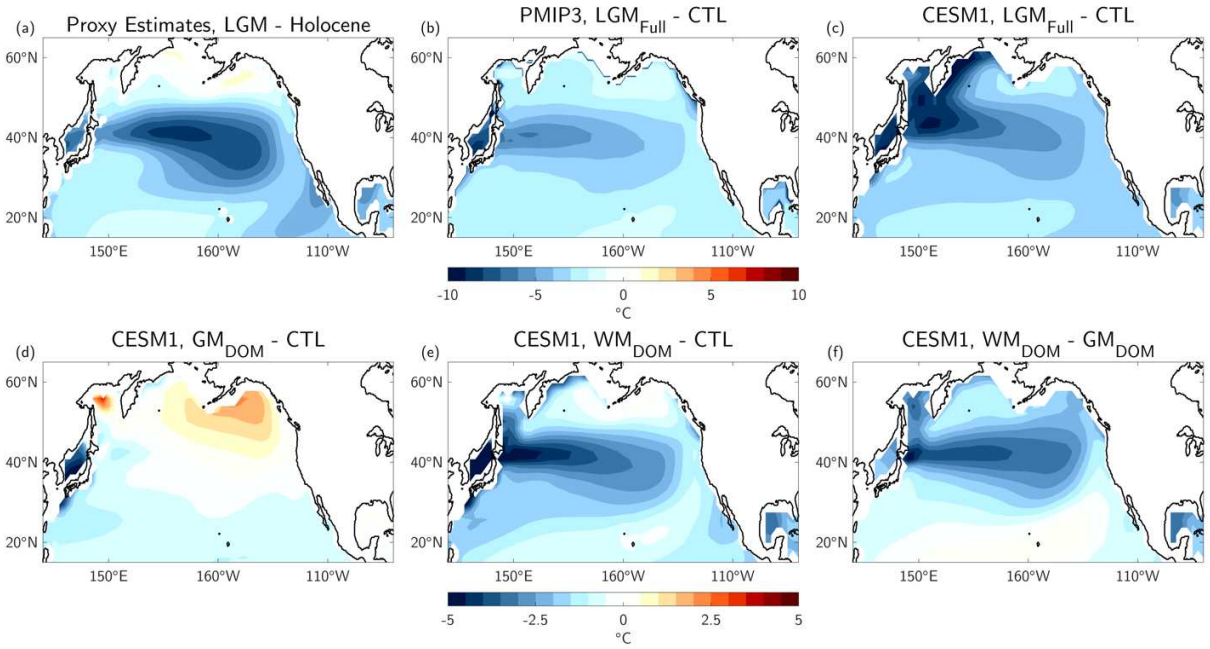

731

732 **Figure 5** Simulated ocean temperature response. Difference maps of annual mean SSTs (˚C) in
733 (a) LGM minus late Holocene data assimilated proxy estimates from Tierney et al. (2020), (b)
734 the ensemble mean of seven PMIP3 models forced with full LGM boundary conditions minus
735 their respective pre-industrial control simulations, (c) CESM1 LGM_{Full} minus CTL simulations,
736 (d) CESM1 GM_{DOM} minus CTL, (e) CESM1 WM_{DOM} minus CTL, and (f) CESM1 WM_{DOM}
737 minus GM_{DOM}.

738

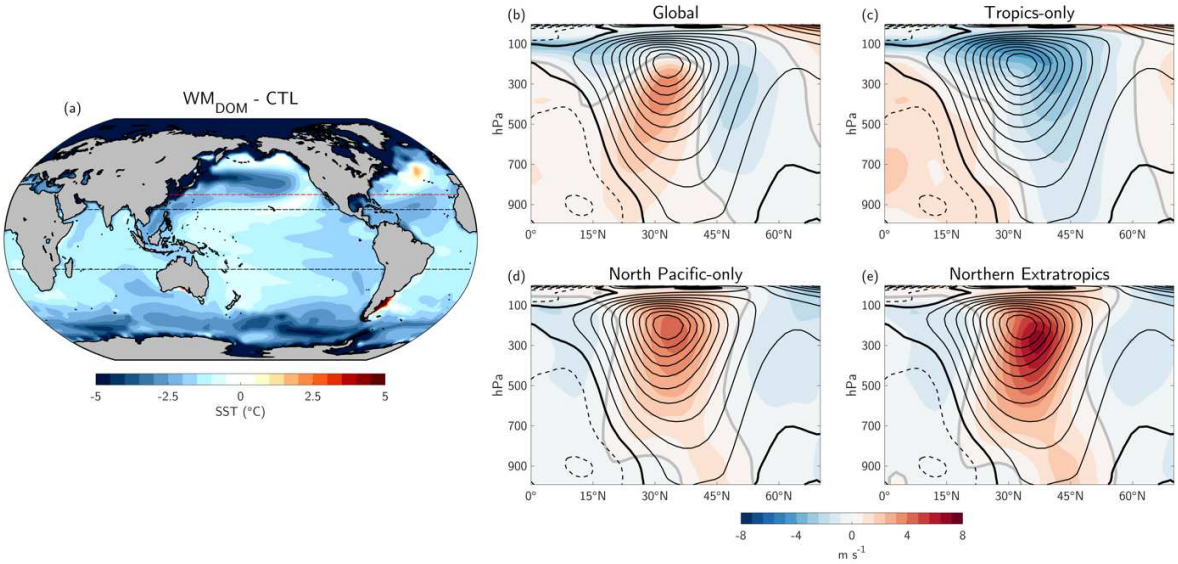

739
740 **Figure 6** North Pacific zonal wind response in WM_{SST}. (a) Global SST anomalies (˚C) for
741 WM_{DOM} minus CTL averaged during December-February. (b)-(e) Latitude-height cross-section
742 of boreal winter (December-February) zonal wind anomalies (shading; m s^{-1}) zonally averaged
743 over the Pacific basin (120˚E-110˚W). Anomalies are from the WM_{SST} CAM5 simulations forced
744 with WM_{DOM} SSTs (b) globally, (c) in the tropics-only (20˚S-20˚N; equatorward of dashed black
745 lines), (d) in the North Pacific-only (>30˚N; poleward of black dashed line in North Pacific), and
746 (e) in the Northern Hemisphere extratropics (>30˚N; poleward of the black dashed line at all
747 longitudes). Black contours in (b)-(e) denote the winter WM_{SST} control zonal wind climatology
748 for this region. Solid (dashed) black contours denote positive (negative) values. Black contour
749 interval is 5 m s^{-1}, with the thick black contour marking 0 m s^{-1}. Thick gray contour marks the 0
750 m s^{-1} zonal wind anomaly contour.
751

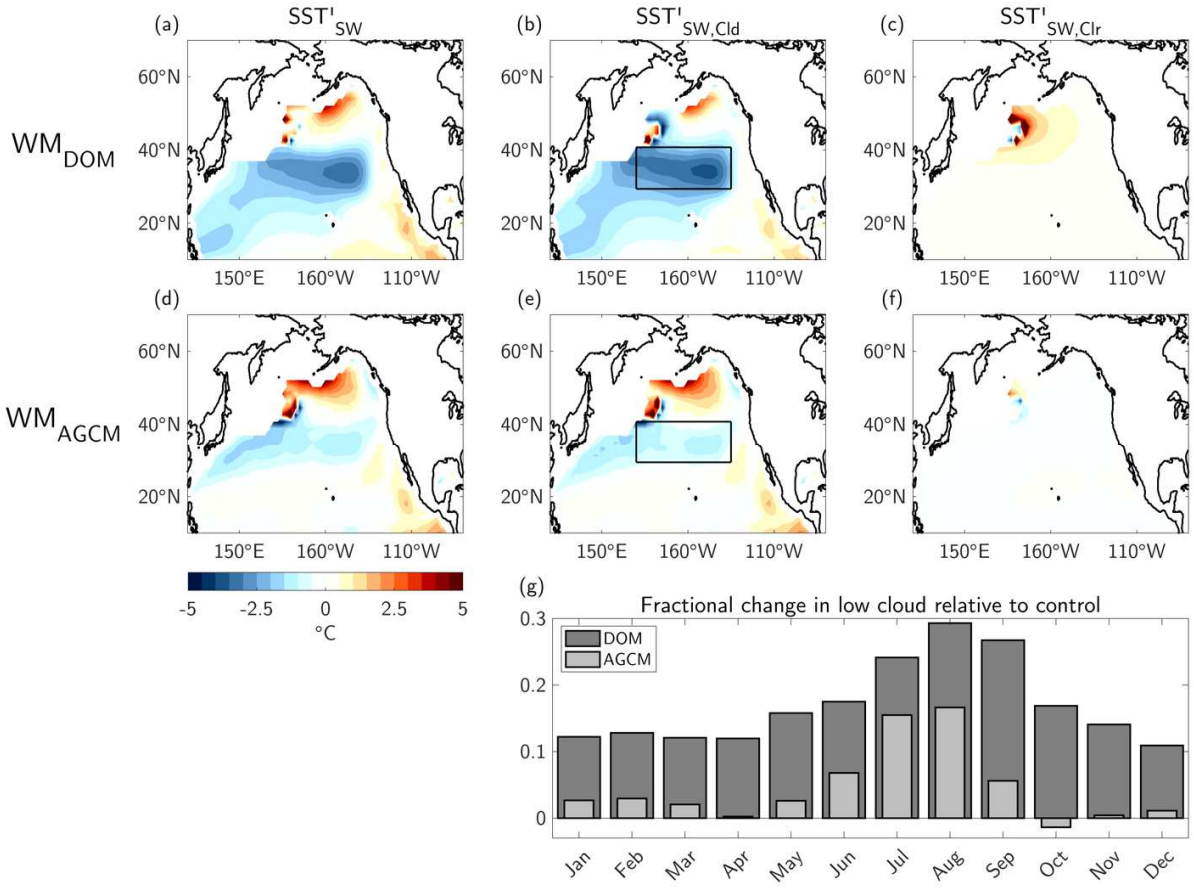

752

753 **Figure 7** Impact of clouds on ocean temperatures. SST anomalies implied by changes in annual
754 mean (a) net surface shortwave, (b) shortwave cloud radiative forcing, and (c) clear-sky surface
755 shortwave in WM_{DOM}. (d)-(f) Same as (a)-(c), but for WM_{AGCM}. (g) Monthly fractional change
756 (relative to CTL) in low cloud amount, averaged in black boxes in (b) and (e) for WM_{DOM} (dark
757 gray) and WM_{AGCM} (light gray).

758

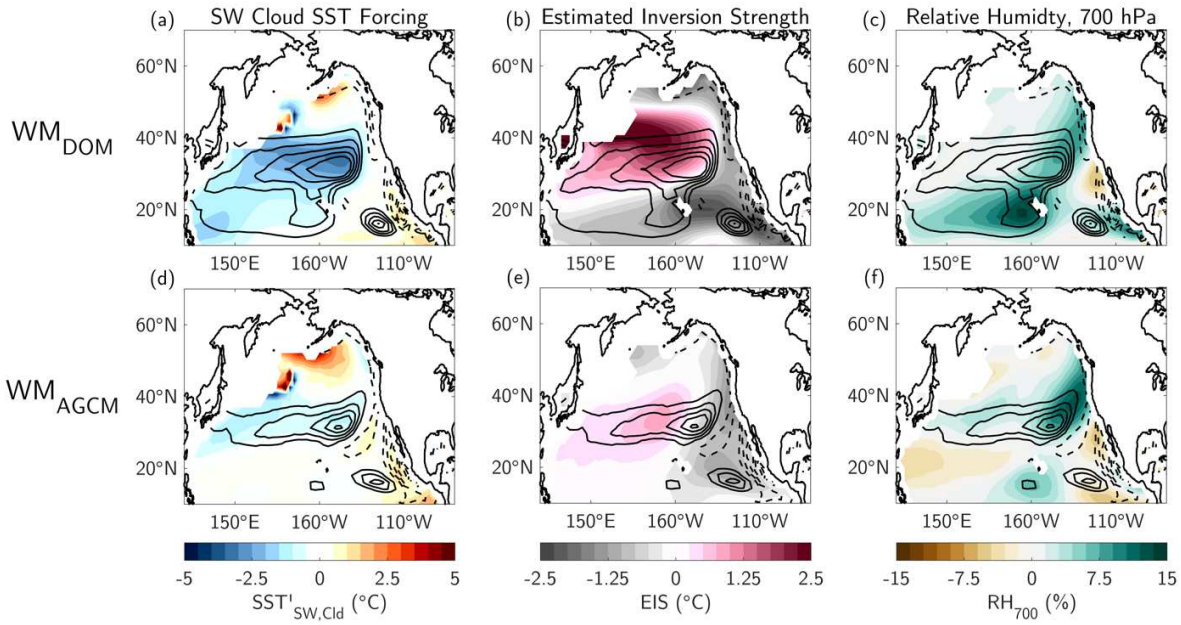

759

760 **Figure 8** Low cloud controlling factors. (left column) SST anomalies implied by changes in
761 annual mean shortwave cloud radiative forcing (shading; ˚C), (middle column) Estimated
762 Inversion Strength (EIS; shading; ˚C) anomalies averaged during boreal summer (June-August),
763 and (right column) relative humidity anomalies (shading; %) at 700 mb averaged during boreal
764 summer in (a)-(c) WM_{DOM} minus CTL and (d)-(f) WM_{AGCM} minus CTL. Black contours in each
765 panel depict the corresponding fractional change in summertime averaged low cloud fraction
766 (e.g., WM_{DOM} minus CTL over CTL). Solid (dashed) black contours denote positive (negative)
767 values. Contour interval is 0.1 starting at 0.1. See Supplementary Materials Section S1.4 for
768 more details on the cloud parameters analyzed here.

769

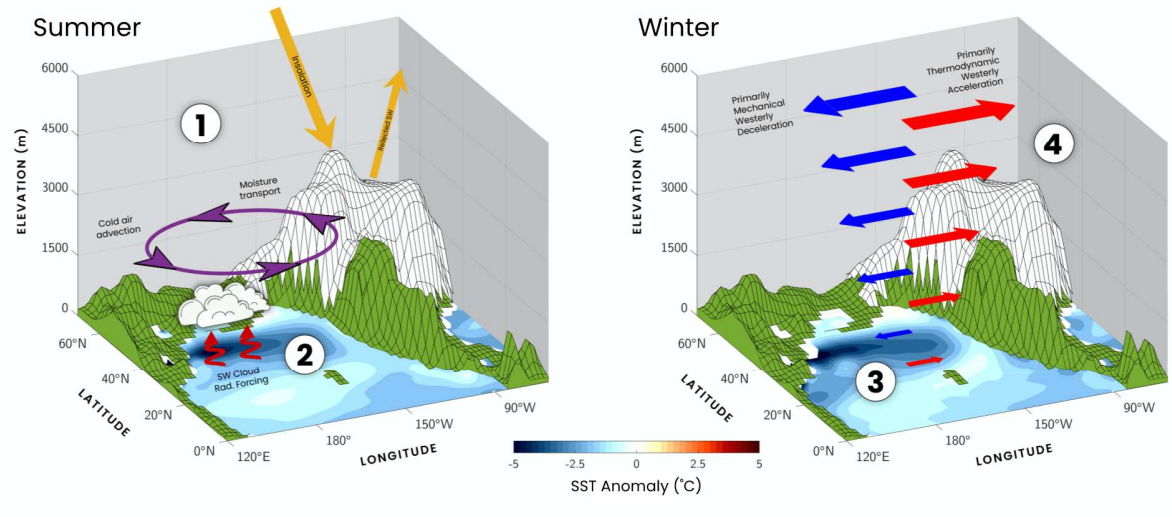

770

771 **Figure 9** Schematic summary of the North Pacific coupled climate response to tall/bright North
772 American ice sheets during the LGM. (1) A direct stationary wave response to the tall/bright ice
773 sheets during boreal summer produces a low-level cyclonic circulation over the North Pacific.
774 These circulation anomalies drive cold air advection in the western North Pacific and increased
775 water vapor transport in the eastern North Pacific. (2) Enhanced stability coupled with increased
776 atmospheric moisture leads to more marine stratocumulus clouds, which reflect sunlight and cool
777 the North Pacific Ocean near ~40˚N. (3) Low cloud-SST feedback and ocean dynamical
778 adjustments amplify the SST and cloud changes, persisting them into boreal winter. (4) The
779 enhanced North Pacific meridional temperature gradient accelerates the westerlies on the
780 equatorward flank of the jet stream, while mechanical interactions with ice sheet topography
781 decelerate the flow on the poleward flank. Overall, this leads to a southward shift of both the
782 North Pacific jet stream and North American west coast hydroclimate during the LGM.